

Multi-Point Nanoindentation Method to Determine Mechanical Anisotropy in Nanofibrillar Thin Films

Dinidu Perera, Qijue Wang, and Hannes C. Schniepp*

Biomaterials with outstanding mechanical properties, including spider silk, wood, and cartilage, often feature an oriented nanofibrillar structure. The orientation of nanofibrils gives rise to a significant mechanical anisotropy, which is extremely challenging to characterize, especially for microscopically small or inhomogeneous samples. Here, a technique utilizing atomic force microscope indentation at multiple points combined with finite element analysis to sample the mechanical anisotropy of a thin film in a microscopically small area is reported. The system studied here is the tape-like silk of the Chilean recluse spider, which entirely consists of strictly oriented nanofibrils giving rise to a large mechanical anisotropy. The most detailed directional nanoscale structure–property characterization of spider silk to date is presented, revealing the tensile and transverse elastic moduli as 9 and 1 GPa, respectively, and the binding strength between silk nanofibrils as 159 ± 13 MPa. Furthermore, based on this binding strength, the nanofibrils' surface energy is derived as 37 mJ m^{-2} , and concludes that van der Waals forces play a decisive role in interfibrillar binding. Due to its versatility, this technique has many potential applications, including early disease diagnostics, as underlying pathological conditions can alter the local mechanical properties of tissues.

nanofibrillar spider silk, which provides unprecedented insight into the mechanics and bonding at the level of nanofibrils. This work deepens our understanding of silk and other fibrous materials, and it will inspire/enhance the future development of synthetic, biomimetic performance materials.^[12–16]

Large-scale synthetic production of a sustainable high-performance material mimicking spider silk has been a goal for a long time.^[17–20] However, matching the outstanding performance of natural silk—generally attributed to its sophisticated, hierarchical structure—has proven very challenging.^[17–21] Details of the structure of silk are still controversially discussed;^[9,22,23] and while there have been corresponding modeling efforts for spider silk,^[9–11] there is currently no experimental evidence available to directly reveal the mechanical interplay of the different components of silk fiber. The latter has hindered tests of the models, and thus, a

detailed understanding of the origins of performance of silk-like fibers, as well as their successful synthetic implementation. Recently, the role of nanofibrils as crucial structural elements in these materials has become increasingly clear.^[1,23–26] This work shows that the mechanical anisotropy of silk holds the key to understanding the interaction between silk nanofibrils, and can thus, advance the understanding of silk mechanics. Our previous work hinted that the adhesion between the nanofibrils in a silk fiber is weak compared to their tensile strength.^[24] However, due to their microscale dimensions, quantitative characterization of mechanical anisotropy in silk fibers has been limited to measurements of the modulus using atomic force microscopy (AFM) indentation^[27] and Brillouin scattering.^[28] However, without knowing the strength, little can be said about binding energies and the material behavior in the high-strain regime, where silk is particularly interesting, as it features significant plastic deformation and excels with outstanding toughness.

Generally, mechanical anisotropy at micro- and nanometer length scales is challenging to measure.^[29–32] A few techniques have been proposed to characterize thin films with microscale lateral dimensions.^[33–37] The combined wrinkling–cracking method developed by Chung and coworkers uses an elastomeric substrate to support a thin film and stretch the substrate to strain the film.^[33] However, this method suffers from several limitations such as the inability to produce stress–strain relationship over the full strain range of the material. It also

1. Introduction

Oriented nanofibrils play a key role in an overwhelming number of biomacromolecular materials including wood and cartilage (collagen).^[1–3] Nanofibrils also have been considered the basic structural element in spider silk, suggested to give rise to the superior mechanical properties of this outstanding biomaterial.^[4–8] A more detailed understanding of the structure–property relationships at the level of nanofibrils would be desirable. While modeling methods have been developed to study such materials at the nanofibrillar/mesoscopic level,^[9–11] there is a lack of suitable experimental techniques to test these theories directly and further advance the field. Especially, the mechanical properties and interfacial interactions of nanofibrils have not yet been characterized, which is difficult because of the small size of silk fibers. Here, we report the first method to directly measure the stiffness and strength anisotropy of

D. Perera, Q. Wang, H. C. Schniepp
Department of Applied Science
William & Mary
P.O. Box 8795, Williamsburg, VA 23187-8795, USA
E-mail: schniepp@wm.edu

 The ORCID identification number(s) for the author(s) of this article can be found under <https://doi.org/10.1002/sml.202202065>.

DOI: 10.1002/sml.202202065

requires an elastomeric substrate that is mechanically stronger than the tested material and that simultaneously provides high adhesion with the tested material. Most fracture toughness measurement methods based on nanoindentation are developed specifically for brittle films and demand the precise determination of the crack length, which could be challenging for micro- or nanoscale cracks.^[34,35] These experimental methods and their models have been developed only for the isotropic case. Also, they have significant other limitations such as a requirement to employ a supporting substrate of approximately the same stiffness as the film.^[36,38–41] Acoustic techniques, such as the guided-wave elastography used by Li and Cao, monitor the speed of sound propagation within soft tissues and use complex theoretical models to extract the mechanical properties of the material.^[37] However, these techniques and most other methods, such as light scattering used by Koski and coworkers,^[28] are limited to characterizing the elastic properties of the material; none of these techniques have been shown to determine the anisotropy in the regime where plastic deformation or failure occurs. In particular, none of the previous techniques has characterized strength anisotropy.

Here, we introduce a generally applicable method that combines a novel AFM-based indentation technique on suspended films with finite element analysis (FEA) to characterize the mechanical properties of anisotropic thin films over a large strain range including plasticity and ultimate strength. We successfully utilize this method to characterize the silk of the Chilean recluse spider (*Loxosceles laeta*). While this silk features mechanical properties comparable to most cylindrical spider silks, it comes in the shape of a high-aspect-ratio ribbon, 40–60 nm thin and 6–8 μm wide, and thus meets the geometric requirements of our experimental technique. Each ribbon is completely made out of axially oriented 20 nm diameter nanofibrils, giving rise to anisotropic mechanical properties.^[24] In this study, we quantified the degree of anisotropy of elastic modulus and strength of the recluse silk to provide new insights into the mechanical interplay between silk nanofibrils. We have also estimated the adhesion strength between spider silk nanofibrils for the first time, which will benefit the development of high-performance synthetic materials inspired by spider silk.

2. Results and Discussion

We suspended the ribbon silk of a recluse spider (Figure 1a) flat over circular, 2 μm diameter holes in a silicon nitride substrate, effectively making circular silk membranes constrained at their perimeter. We identified well-suspended and adhered regions using both optical microscopy (Figure 1b) and AFM tapping mode imaging (Figure 1c). The AFM image confirmed that the silk adhered and conformed so well to the substrate that the substrate's intrinsic roughness could be observed on top of the ribbon (Figure S1, Supporting Information). This roughness was absent in the suspended area of the ribbon (highlighted by the dashed circle), which helped us to identify the position of the hole in the AFM images. The silk ribbon, and therefore, the silk nanofibrils (also visible in Figure 1c), were oriented vertically (γ -direction in Figure 1b,c).

Force spectroscopy was then carried out on the suspended silk membrane using the same dynamic-mode AFM probe first used for imaging, but this time in static mode to measure the membrane's indentation response. In contrast to previous experiments with suspended graphene^[42] and hexagonal boron nitride,^[43] which were carried out at the central location P_0 , we also performed experiments at locations P_x and P_y at a separation of only 100 nm from the rim. These positions were chosen such that the internal nanofibrils in the silk tape were oriented parallel (P_x) or perpendicular (P_y) to the rim, with the goal to expose the mechanical anisotropy resulting from the fibril orientation.

First, we explored the small-strain, elastic regime of the material, where the total indentation depth was limited to 50 nm. At each of the three locations P_0 , P_x , and P_y , five approach/retract curves were acquired at each point. The obtained force-versus-displacement curves were converted to force-versus-membrane deformation (see Experimental Section); representative curves are shown in Figure 1e as solid lines. Force curves taken close to the rim (P_x and P_y) featured much higher slopes compared to the central indentation at location P_0 . This is in line with expectations since the membrane is less constrained in the center and thus, softer. Interestingly, location P_y featured an even higher slope than P_x , although both points had the same separation from the rim. This indicates the anisotropic behavior of the material. To further understand the origin of the observed difference, we carried out FEA for this geometry.

We implemented an FEA model of a thin circular disk with linear-elastic, anisotropic bending and stretching capabilities using Salome-Meca.^[44] Due to the relative thinness of the ribbon—40 to 50 nm, small compared to the 2 μm diameter of the suspended circular area—we employed a shell model.^[45] The disk was constrained at the perimeter in all degrees of freedom (displacements and rotations, i.e., clamped boundary condition). The impact of our AFM probe in the experiments was modeled by applying a vertical downward force over a circular area with a radius of 75 nm, in agreement with measured tip dimensions post-indentation (Figure S2, Supporting Information). FEA results for indentations at locations P_x and P_y are shown in Figures 2a,b, respectively, where the vertical deformations are represented using the same color scale. In order to model anisotropic material properties as suggested by our experimental results, we employed a significantly softer modulus in the direction perpendicular to the nanofibrils, $E_x = 1$ GPa, than parallel to the nanofibrils, $E_y = 9$ GPa, for our simulations. The simulations also require knowledge of the Poisson ratio ν of the tested material; however, experimental data of ν for silks is scarce and without a clear consensus.^[28,46,47] We found that ν does not dramatically affect the outcome of the simulations, and we assumed $\nu = 0.4$ (isotropic) in our simulations. Most notably, both the indentation depths and deformation patterns are significantly different for indentation locations P_x and P_y . In terms of our model, the only difference between the two locations is that at P_x (Figure 2a), the softer material direction x is perpendicular to the rim, whereas, at P_y (Figure 2b), the stiffer material direction y is perpendicular to the rim. Evidently, the material anisotropy $E_y > E_x$ caused an observable difference in indentation depth. In other words, it is

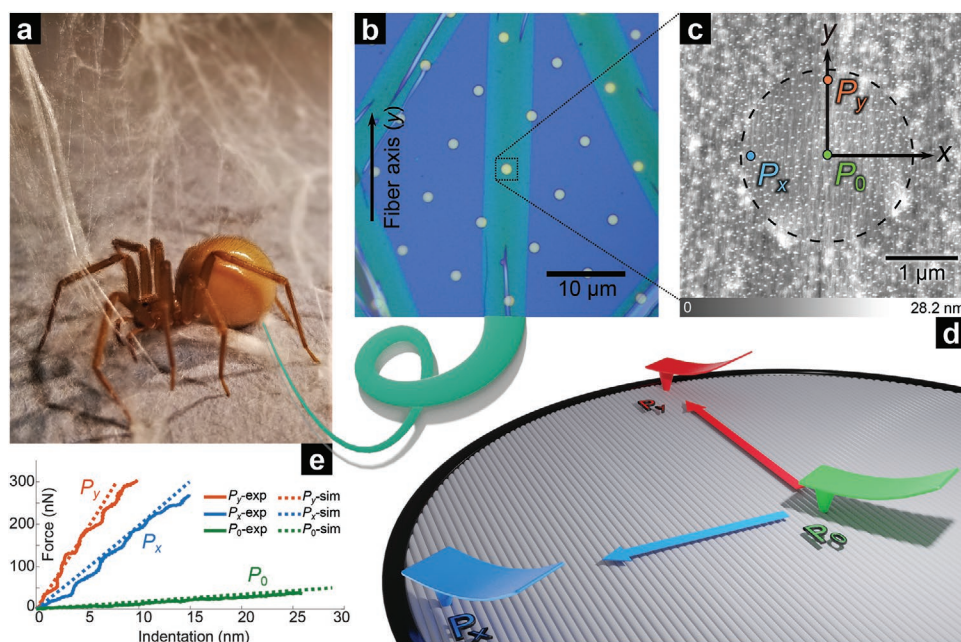


Figure 1. a) A Chilean recluse spider surrounded by its silk. b) Optical micrograph of tape-like recluse silk flattened on a Si_3N_4 substrate featuring $2\ \mu\text{m}$ diameter circular holes. c) Tapping-mode AFM image of a silk membrane suspended over a hole. The two axes x , y , and the indentation positions are marked on the image. d) 3D rendered illustration of the suspended silk membrane showing the indentation positions relative to the direction of the nanofibrils. e) Experimental versus simulated force curves for small indentations at P_y , P_x , and P_0 .

generally possible to detect material anisotropy by means of a simple vertical indentation experiment, if carried out at suitable locations of the suspended membrane.

To quantify the impact of the anisotropic modulus $E_{x/y}$ on the indentation experiments, we systematically varied E_x and E_y in our simulations and found that the ratio of indentation depths at the two different locations, $(P_y/P_x)^{-1}$, only depends on the ratio $\eta = E_y/E_x$ of transverse and longitudinal elastic modulus. In Figure 2c, we show $(P_y/P_x)^{-1}$ as a function of $\eta = E_y/E_x$, which increases strictly monotonically and thus demonstrates that quantitative measurement of the degree of anisotropy η is feasible. The actual sensitivity depends on the experimental geometry (diameter of the suspended region, separation from rim, and the size of the AFM probe). In our experiments, $(P_y/P_x)^{-1} \approx 1.92$ (see Figure 1e), corresponding to $\eta \approx 9$ (see the red asterisk in Figure 2c). In our case, the axial elastic modulus of the ribbons had already been determined via tensile testing

to be $E_y = 9\ \text{GPa}$; correspondingly, the lateral elastic modulus was $E_x = 1\ \text{GPa}$; and Figures 2a,b represent these $E_{x/y}$ values. The same set of $E_{x/y}$ values also fit our experimental results at positions P_0 , P_x , and P_y successfully (dotted lines in Figure 1e). The measured tensile elastic modulus ($E_y = 9\ \text{GPa}$) of recluse silk is comparable to most major ampullate cylindrical spider silks.^[6] However, the measured transverse elastic modulus ($E_x = 1\ \text{GPa}$) is significantly below the values reported previously via indentation tests on silk surfaces of different orientations ($6\text{--}7\ \text{GPa}$)^[27] and Brillouin scattering ($5\text{--}15\ \text{GPa}$).^[28] However, we believe it is possible that these prior experiments overestimated the lateral modulus. For indentation experiments, it is difficult to decouple the spatial directions without mechanical modeling; the Brillouin experiments featured significant scatter in the experimental data. Therefore, our findings suggest that the mechanical anisotropy of nanofibrillar silk is much higher than previously thought. The entirely nanofibrillar ribbon

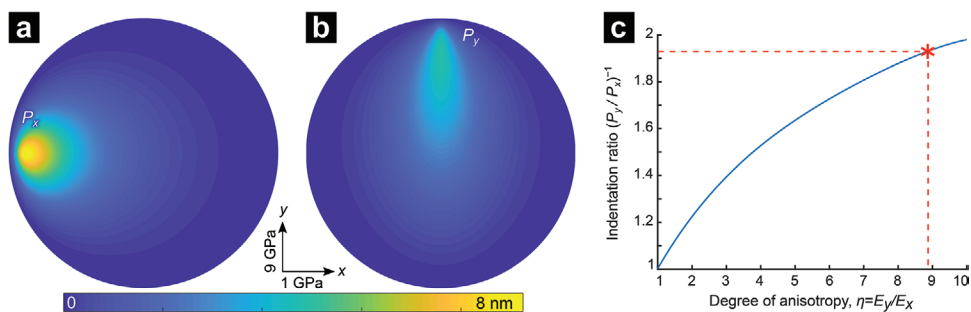


Figure 2. FEA results showing different deformations at a) P_x and b) P_y for an identical indentation force when there is a 1:9 degree of elastic modulus anisotropy between the x and y directions. The color bar provides a joint calibration of vertical deformations in (a,b). c) Ratio between the indentations at P_x and P_y versus degree of anisotropy $\eta = E_y/E_x$. Red dashed lines and asterisk represent experimental results obtained for recluse silk.

silk of the recluse spider has proven to be the ideal system to explore these unique mechanical properties.

So far, we have explored the mechanical anisotropy of spider silk in the low-strain regime, which allowed us to determine the anisotropy of the elastic modulus. Much more difficult and critically important to understand the material's behavior is the anisotropy in strength; however, this is experimentally much more challenging and has not been previously accomplished for spider silk. In particular, this requires exploring the high-strain regime of the material, where it is subject to plastic deformation. Describing this inelastic, nonlinear material regime in the realm of anisotropic materials is still subject to ongoing research and is highly complex,^[48–50] hence, not yet implemented in commonly used FEA packages. We explored this regime experimentally by force spectroscopy of increasing indentation depths, to the point of failure of the suspended membrane.

Figure 3a shows a representative series of four measured indentations of increasing depth, which were carried out at the P_x position, 170 nm from the rim. In this case, we distinguish between approach (blue shades) and retract curves (red shades). The chosen indentation depths (80, 125, 170, and 200 nm) were significantly larger than in our previous low-strain experiments (Figure 1e), and consequently caused plastic deformation of the silk membrane. Due to this plastic deformation, the shape of the blue indentation curves systematically changed in the series of indentations 1–4. The linear-elastic model for the deformation of an anisotropic membrane is shown as a dotted, blue curve. (The apparently nonlinear, upward bending characteristic of this curve is due to the “drum” geometry of this system.) The first experimental indentation curve (dark blue) follows this model for small indentations, but then shows a lower slope, indicating significantly nonlinear behavior of the material. The same behavior is observed in tensile testing of silk fibers^[7] and can be explained with strain hardening,^[51] which has been observed in silk.^[52] From this strain hardening point of view, the material is expected to undergo plastic deformation; this is in line with our experimental results (Figure 3a), where the retract curve 3' shows a lower force than the corresponding approach curve 3 at any indentation, indicating that the sample was permanently stretched during the approach. The same is true for the approach/retract pairs 1/1' and 2/2'. (The raw data and detailed explanation of the data processing are shown in the Supporting Information.) The strain-hardening picture is further confirmed by the fact that the second approach curve shows a higher slope than the first curve for indentations of 50 nm and above. Only after exceeding 80 nm, the maximum indentation of the first curve, the slope of the second curve start to decrease. This behavior indicates continued plastic deformation and yield of the material as expected according to the strain-hardening model. The third approach curve continues these trends accordingly. The fourth approach curve (lightest blue shade) initially also follows the same trend. However, it does not extend into higher forces; instead, the stresses peak at an indentation of ≈ 173 nm (185 ± 12 nm for all datasets) and decrease afterward, indicating failure of the membrane. This was confirmed by post-mortem scanning electron microscope (SEM) imaging (Figure 3b). The complete details of data analysis, representation, and offsets introduced are shown in Figure S4, Supporting Information.

In contrast to the approach curves 1–4, the corresponding retract curves 1'–4' of our force spectroscopy experiments (red shades) are very similar in shape. To highlight this similarity, the retract curves 1' and 2' in Figure 3a were shifted to the right to overlap with the retract curve 3'. The horizontal dotted lines connect the initial (circles with blue shades) and shifted (circles with red shades) beginnings of each retract curve and simultaneously represent the amount of plastic deformation between the indentations 1 and 3 as ≈ 70 nm (long horizontal dotted line), and indentations 2 and 3 as ≈ 45 nm (short horizontal dotted line). The near-perfect overlap between all retract curves is fully in line with a strain-hardening model, where it is expected that the relaxation of a strained specimen reflects only the elastic properties of the material; the relaxation curves thus do not depend on the previous history of straining, other than changes to the length of the specimen due to plastic deformation. Most notably, the elastic experimental retract curves are in very good agreement with our model assuming an anisotropic, linear-elastic material represented by the red dotted curve in Figure 3a. (This red dotted curve is an extended, right-shifted version of the blue dotted curve in the same figure.)

The observed elastic relaxation behavior turned out to be critically important in the analysis of the anisotropic properties of spider silk, which is a plastic material. Characterization, in this case, is challenging, since both the elastic and plastic behavior of the material can be orientation-dependent (anisotropic), which requires the determination of at least two parameters for each spatial direction. Obtaining a total of four parameters for the x and y directions of the silk ribbon via indentation in the z -direction is challenging. By focusing on the retract curves, we were able to neglect plasticity, and our linear-elastic anisotropic model of the material became applicable over the entire strain regime. This approach allowed us to determine the direction-dependent stresses at failure, and ultimately, the strength anisotropy of the material.

Our indentation experiments showed that mechanical failure of the silk tapes is always accompanied by a breakdown of the adhesive contact between nanofibrils. This became evident after reviewing post-mortem SEM images like the one shown in Figure 3b and agrees with our previous findings.^[24] Correspondingly, the lateral stress σ_x in the direction perpendicular to the fibrils (x -direction in Figure 2) at the moment of failure (at an indentation depth of ≈ 173 nm in Figure 3a) is the adhesive strength between the fibrils, determining the lateral tensile strength $\sigma_{TS,x}$ of the material. We found that $\sigma_{TS,x} \approx 159 \pm 13$ MPa, which is the first measurement of the lateral strength of a material entirely consisting of parallel nanofibrils. Hence, the transverse strength of recluse silk is only around 1/5th of its tensile strength, fully supporting our hypothesis that this material has highly anisotropic mechanical properties.^[24]

Interestingly, this work further allows us to deduce the strength of interaction forces at the level of individual nanofibrils. This information is critically important for the development of mechanical models of such nanomaterials, which not only take into account their observed macroscopic properties but also use evidence-based parameters to describe properties and interactions of individual, nanoscale constituents. First, we wanted to find the adhesive force per unit length between

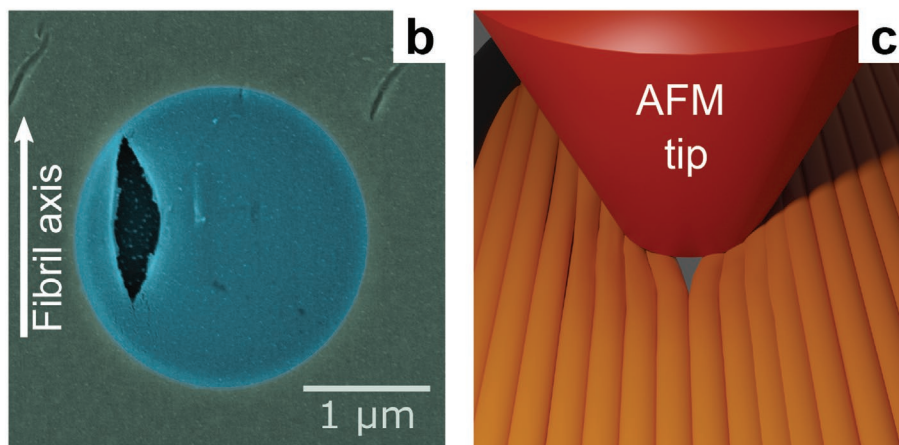
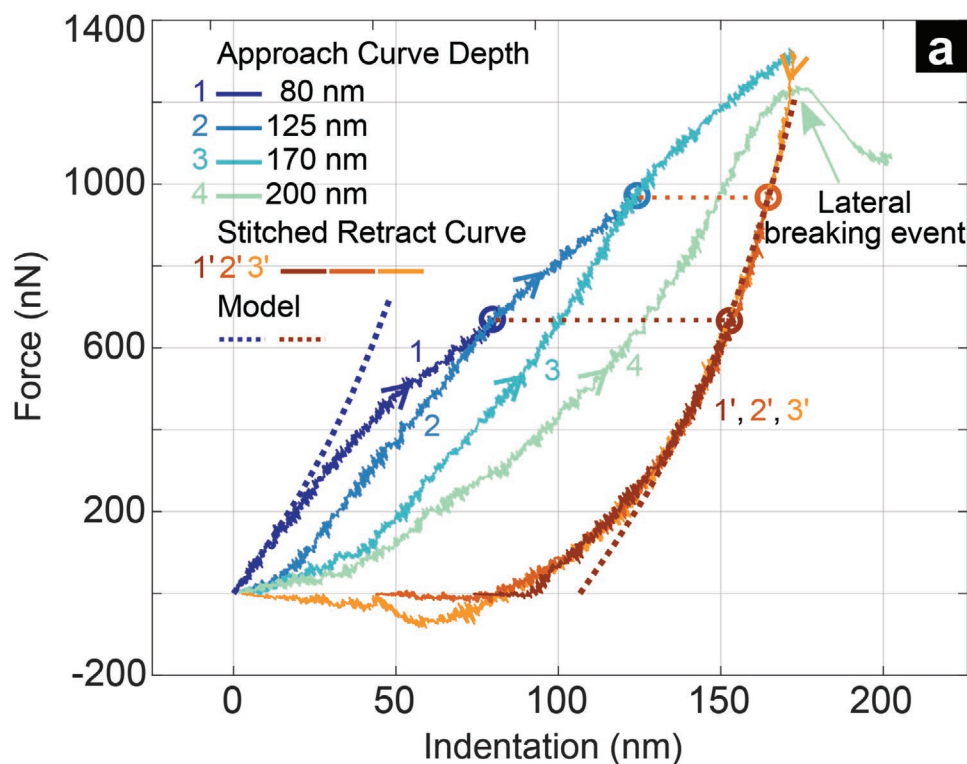


Figure 3. a) Relationship between the applied force and the vertical membrane deformation. Solid lines represent the experimental curves obtained by four sequential nanoindentations conducted by increasing the vertical indentation. Blue shades are approach curves and red shades are retract curves. Dashed lines represent the corresponding simulated curves. b) SEM image of silk membrane ruptured along the fibril orientation. c) Illustration of membrane failure by disjoining of nanofibrils due to the force applied by the AFM tip.

two nanofibrils φ_{adh} . Collective interactions of close-packed nanofibrils within the silk ribbon complicate this calculation. Based on our detailed analysis of the geometry of close-packed nanofibrils (Figure S5, Supporting Information), we estimated the adhesive force per unit length in between two nanofibrils as $\varphi_{adh} = 1.84 \text{ N m}^{-1} = 1.84 \text{ nN nm}^{-1}$. After that, we used a Johnson–Kendall–Roberts (JKR)-based model^[53] to describe the contact mechanics of elastic cylinders (Figure S6, Supporting Information) and further converted this breaking force into a corresponding surface energy γ and obtained $\gamma = 37 \text{ mJ m}^{-2}$. This surface energy is in very good agreement with silk surface energies determined by Zhang et al. via inverse gas chromatography

(IGC), 42–47 mJ m^{-2} .^[54] (The details of these calculations are shown in the Supporting Information.)

Having established that the breaking forces between nanofibrils and the corresponding surface energies are relatively low, we wanted to know the origin of the interfibrillar binding forces. In their surface energy measurements, Zhang et al. were explicitly interested in the relative contributions of van der Waals forces and hydrogen bonding to the surface energy and correspondingly did IGC experiments with different probe molecules.^[54] They concluded that the bulk of the observed surface energy was due to dispersion forces, with H-bonds only playing a minor role. The surface energy we observed is

similar to the value they observed, which might indicate that the nanofibrils in a *Loxosceles* ribbon are mainly held together by van der Waals forces.

Our findings for the *Loxosceles* silk are interesting to discuss in the context of other silks. While recluse silk is unique in terms of its ribbon morphology, there is an increasing amount of evidence showing that other silks share its makeup on the mesoscale: a bundle of uniform, parallel nanofibrils. For instance, it has recently been shown that fibers from the silkworm *Bombyx mori* can be fully “exfoliated” into nanofibrils without destroying the nanofibrils’ integrity.^[55,56] We believe that this observation reflects the similarity of *B. mori* with recluse silk that is shared with many other silks and nanofibrillar materials in general, leading to a correspondence between binding potential asymmetry and mechanical anisotropy. The weaker interfibrillar forces, likely only van der Waals type, lead to a lower lateral Young’s modulus and breaking force; the stronger intra-fibrillar binding forces, covalent within the protein and H-bonding between proteins, translate into a larger axial modulus and strength.

The level of detail obtained from our experiments can be used to test existing models of silk and to inform new ones. Some models aimed to represent the mesoscale structure of silk including proposals for molecular-scale mechanisms and interactions to match the observed elastoplastic tensile behavior of silk.^[9–11] Such models can now be refined using the nanofibril dimensions, interactions, and tensile properties^[24] we determined experimentally. Such models could further be tested by comparison with the plastic behavior we observed, and they may be best suited to describe this complicated case of a highly anisotropic material, which is challenging to describe using continuum models.

The observed interfibrillar mechanics may also be important for the functional properties of silk. We imagine that the weak interactions between recluse silk nanofibrils facilitate their ability to slide past each other when the silk fiber is bent or makes turns. This supports our previous conclusion that a silk fiber is similar to a stranded—as opposed to a solid—cable.^[24] Accordingly, the sliding ability is expected to minimize the permanent damages caused by the extreme bending strains^[25] that would be expected in the recluse’s web consisting of a meta-structure with 3–5 loops per millimeter.^[16] This may also apply to cylindrical fibers of orb-weaving spiders featuring a similar nanofibrillar mesostructure, which can undergo sharp turns, for instance, at their surface attachment points. Cylindrical fibers are particularly vulnerable to bending-induced failure due to stress concentration in these turns. In natural spider webs, this premature failure is not observed,^[47] which may very well be due to this stranded cable structure with relatively easily sliding strands, which is in line with the low interfibrillar interaction strengths we observed.

The ability of our method to characterize nanoscale interactions and fundamental materials properties based on measuring micrometer-scale samples opens up new pathways to study the structure–property relationships of materials far beyond silk. For general application, we summarized the steps of our method as a flow diagram shown in Figure S7, Supporting Information. As we demonstrated, our method can be used to measure the surface energies, adhesion, and make

estimates about the nature of underlying forces (van der Waals vs hydrogen bonds). These important nanoscale properties are helpful to obtain a fundamental understanding of nanomechanics of many materials including wood (cellulose), collagen, exoskeletons of arthropods (chitin), and fiber-reinforced synthetic materials. In cases where materials, especially, biological materials, such as soft tissues, cell membranes, and tendons, are not readily available as thin films, established microtoming techniques may be used to obtain them in thin-film form.

Our technique may prove important for medically relevant materials such as cartilage, skin, corneal, and brain tissues.^[57–62] Since the local mechanical variations of biological matter are highly related to underlying pathological conditions,^[57,60–68] our method could potentially be developed for diagnostics. For instance, recent studies have found that mechanical anisotropy is important for the spreading rate of cancers on cell membranes and in soft tissues^[64] and for predicting the effects of traumatic brain injuries.^[66,69] However, these effects have not been researched systematically.

3. Conclusion

In summary, we have developed a technique combining experiments and computer simulations to quantify the anisotropic mechanical properties of thin films locally and on the microscale including elastic modulus and strength. We subsequently used this novel method to show that the mechanical properties of recluse spider silk fibers are highly anisotropic, due to their nanofibrillar structure. The observed transverse elastic modulus of recluse silk was 1 GPa, which is nine times smaller than its longitudinal (tensile) modulus. Importantly, we deduced the mechanical interaction strength of individual silk nanofibrils for the first time. The measured strength, that is, lateral breaking strength was 159 ± 13 MPa, which is about five times lower than the tensile strength of the material. This yielded ≈ 1.84 nN nm⁻¹ as the lateral disjoining force per unit length for two silk nanofibrils. We utilized a model based on JKR theory to calculate the surface energy γ of silk nanofibrils based on the measured disjoining force for two nanofibrils. We found $\gamma = 37$ mJ m⁻², in agreement with the literature, and in support of a hypothesis that inter-fibrillar interactions are dominated by van der Waals forces. We discussed the implications of our findings for other silks. Our observation that spider silk nanofibrils are held together loosely supports a “cable model” of spider silk, in which parallel nanofibrils can easily slide past each other to maintain fiber integrity in the presence of bends or turns.

The advantage of our technique is that it can explore the high-strain regime for loading and unloading of a microscopic sample; hence, it can be used to determine properties such as elastic versus plastic deformation, and stress recovery. For our spider silk samples, we have observed clear evidence of strain hardening, which we believe has great potential to further our understanding of its nanomechanics and structure–property relationships. We believe our work will have a significant impact on the mechanical modeling of silk, where current models can be tested, and advanced models can be developed in the future.

Our method can also be used to study a range of fibrillar materials other than silk including most collagen-based biological matter, wood, and synthetic nanocomposites. It can be further developed as a disease diagnostic method based on local mechanical property variations of biological matter that occur due to underlying pathological conditions. The ability of our method to measure the local mechanical properties allows us to observe the effect of local mechanical property variations on the global mechanical and functional properties of the material. Thus, it will generate new pathways for novel disease diagnostic methods and developments of bio-inspired high-performance materials.

4. Experimental Section

Spider Care and Sample Preparation: Chilean recluse spiders (*L. laeta*) were kept individually in cylindrical capsules and fed a weekly diet of crickets. A cotton strip was placed inside the capsules to help the spiders make silk. For indentation experiments, this naturally spun silk was placed on a Si₃N₄ substrate (DuraSiN, EDEN Instruments) featuring holes with a 2 μm diameter distributed on the surface in a square pattern featuring a 10 μm pitch (Figure 1b). Using an optical microscope, it was possible to identify locations where the holes were completely covered by the silk ribbon.

AFM Imaging and AFM Force Spectroscopy: A Ntegra Prima AFM (NT-MDT) system with a 100 μm × 100 μm × 10 μm closed-loop piezo scanner was employed for dynamic-mode imaging and to acquire force curves. After identifying the approximate location of the holes using optical microscopy, the area was imaged using dynamic-mode AFM tips (HQ: NSC15/Al BS, μmasch) featuring a radius of curvature $r = 8$ nm, a resonance frequency $f = 325$ kHz, and a spring constant $k = 40$ Nm⁻¹ (nominal values) to accurately determine the hole position. Then, the sharp AFM tip was blunted by pressing against a hard substrate to obtain a tip with a defined geometry of finite size. This dynamic-mode cantilever with a blunted tip was then used to obtain multiple force curves sequentially at a rate of 1 Hz (1 approach/retract cycle per second), recording both approach and retract curves. Afterward, the tip was scanned over a calibration grating (NT-MDT TGT-1) to obtain the shape and the radius of the apex of the blunted tip (Figure S2, Supporting Information), an important parameter required for numerical simulations. Multiple samples were characterized following the same procedure and all yielded comparable results.

The actual spring constants of AFM cantilevers were measured using Sader's method^[70] and were in the range of 10–15 N m⁻¹. Based on these values, effective spring constants were calculated following the method of Heim and coworkers to compensate for the 15° cantilever tilt.^[71,72] Furthermore, since the contact point of the AFM tip was not directly under the edge of the cantilever, another correction to the spring constant was carried out. To calibrate the deflection sensitivity of the AFM, the inverse optical lever sensitivity was calculated by acquiring force curves directly on a hard substrate and determining the slope of the constant compliance region.^[73] Using these values individually determined for each probe, the raw deflection–extension curves were converted to force–distance curves^[73] to obtain the relationship between the applied force and the membrane deformation.

Scanning Electron Microscopy: A Hitachi S-4700 field emission scanning electron microscope (FESEM) equipped with a secondary electron detector was used to image laterally broken recluse silk membranes. The samples were run at an acceleration voltage of 10 kV with a 7.5–8.0 mm working distance. After AFM indentation experiments, the sample was attached to an aluminum SEM sample holder via conductive tape. To prevent charging, the sample was sputter coated (Anatech LTD, Hummer 6.2) with a ≈2 nm layer of gold/palladium prior to FESEM imaging.

FEA Simulations: FEA was conducted using Salome-Meca, an open source software.^[44] The Salome-Meca package was chosen because it

was one of the few available FEA systems capable of addressing both nonlinear analysis and mechanical anisotropy. The suspended silk was modeled as a clamped circular disk with a diameter of 2 μm using an orthotropic 3D-shell model with a thickness of 47 nm (thickness of the silk ribbon measured by AFM topographic line scans). The AFM tip was modeled as a flat cylinder by applying uniform pressure over a circular area, using the experimentally determined radius of the tip (75 nm, see Figure S2, Supporting Information). This force was applied at locations P_y , P_x , and P_0 , matching the experimental conditions. For each indentation location, an optimized mesh was created featuring 2950 second-order triangular elements, containing 5657 nodes. The surface deformation profiles and force-versus-membrane deformation curves were extracted from the FEA simulations (see Figure S3, Supporting Information, for more details).

Statistical Analysis: The raw deflection–extension curves were transformed into force–distance curves using established techniques that are universally used in the field.^[73] All data analysis was implemented in MATLAB. The raw data, codes, along with explanations of all methods used for data analysis have been published in a data repository.^[74] All values were expressed as mean ± standard error, and no further statistical analysis has been used.

Supporting Information

Supporting Information is available from the Wiley Online Library or from the author.

Acknowledgements

This material is based upon work supported by the National Science Foundation under Grant Nos. DMR-1905902, DMR-2105158, and DMR-1352542.

Conflict of Interest

The authors declare no conflict of interest.

Authors Contribution

D.P. carried out force spectroscopy experiments, FEA, data analysis, and interpretations. Q.W. contributed to force spectroscopy experiments and FEA. D.P. and H.C.S. wrote the manuscript. H.C.S. conceived and oversaw the work.

Data Availability Statement

The data that support the findings of this study are openly available in Harvard Dataverse at <https://doi.org/10.7910/DVN/LUEV5J>, reference number 74.

Keywords

atomic force microscopy nanoindentation, local mechanical anisotropy, nanomechanics, silk nanofibrils, silk surface energy, spider silk, strength anisotropy

Received: April 1, 2022

Revised: May 26, 2022

Published online:

- [1] S. Ling, W. Chen, Y. Fan, K. Zheng, K. Jin, H. Yu, M. J. Buehler, D. L. Kaplan, *Prog. Polym. Sci.* **2018**, *85*, 1.
- [2] S. E. Naleway, M. M. Porter, J. McKittrick, M. A. Meyers, *Adv. Mater.* **2015**, *27*, 5455.
- [3] W. Yang, M. A. Meyers, R. O. Ritchie, *Prog. Mater. Sci.* **2019**, *103*, 425.
- [4] L. Römer, T. Scheibel, *Prion* **2008**, *2*, 154.
- [5] L. Eisoltd, A. Smith, T. Scheibel, *Mater. Today* **2011**, *14*, 80.
- [6] I. Agnarsson, M. Kuntner, T. A. Blackledge, *PLoS One* **2010**, *5*, e11234.
- [7] F. Vollrath, D. P. Knight, *Nature* **2001**, *410*, 541.
- [8] J. G. Hardy, L. M. Römer, T. R. Scheibel, *Polymer* **2008**, *49*, 4309.
- [9] S. Keten, Z. Xu, B. Ihle, M. J. Buehler, *Nat. Mater.* **2010**, *9*, 359.
- [10] T. Giesa, M. Arslan, N. M. Pugno, M. J. Buehler, *Nano Lett.* **2011**, *11*, 5038.
- [11] A. Nova, S. Keten, N. M. Pugno, A. Redaelli, M. J. Buehler, *Nano Lett.* **2010**, *10*, 2626.
- [12] J. A. Kluge, O. Rabotyagova, G. G. Leisk, D. L. Kaplan, *Trends Biotechnol.* **2008**, *26*, 244.
- [13] C. Allmeling, A. Jokuszies, K. Reimers, S. Kall, P. M. Vogt, *J. Cell. Mol. Med.* **2006**, *10*, 770.
- [14] F. G. Omenetto, D. L. Kaplan, *Science* **2010**, *329*, 528.
- [15] F. Vollrath, D. Porter, *Soft Matter* **2006**, *2*, 377.
- [16] S. R. Koebley, F. Vollrath, H. C. Schniepp, *Mater. Horiz.* **2017**, *4*, 377.
- [17] M. Widhe, J. Johansson, M. Hedhammar, A. Rising, *Biopolymers* **2011**, *97*, 468.
- [18] X.-X. Xia, Z.-G. Qian, C. S. Ki, Y. H. Park, D. L. Kaplan, S. Y. Lee, *Proc. Natl. Acad. Sci. USA* **2010**, *107*, 14059.
- [19] A. Lazaris, *Science* **2002**, *295*, 472.
- [20] H. Chung, T. Y. Kim, S. Y. Lee, *Curr. Opin. Biotechnol.* **2012**, *23*, 957.
- [21] A. Heidebrecht, L. Eisoltd, J. Diehl, A. Schmidt, M. Geffers, G. Lang, T. Scheibel, *Adv. Mater.* **2015**, *27*, 2189.
- [22] Q. Wang, H. C. Schniepp, *JOM* **2019**, *71*, 1248.
- [23] A. Spohner, W. Vater, S. Monajembashi, E. Unger, F. Grosse, K. Weisshart, *PLoS One* **2007**, *2*, e998.
- [24] Q. Wang, H. C. Schniepp, *ACS Macro Lett.* **2018**, *7*, 1364.
- [25] C. Fu, Y. Wang, J. Guan, X. Chen, F. Vollrath, Z. Shao, *Mater. Chem. Front.* **2019**, *3*, 2507.
- [26] F. Vollrath, T. Holtet, H. C. Thøgersen, S. Frische, *Proc. R. Soc. B: Biol. Sci.* **1996**, *263*, 147.
- [27] D. M. Ebenstein, K. J. Wahl, *J. Mater. Res.* **2006**, *21*, 2035.
- [28] K. J. Koski, P. Akhenblit, K. McKiernan, J. L. Yarger, *Nat. Mater.* **2013**, *12*, 262.
- [29] M. F. Pantano, H. D. Espinosa, L. Pagnotta, *J. Mech. Sci. Technol.* **2012**, *26*, 545.
- [30] R. Agrawal, H. D. Espinosa, *J. Eng. Mater. Technol.* **2009**, *131*, 041208.
- [31] M. A. Haque, T. Saif, in *Springer Handbook of Experimental Solid Mechanics*, Springer, New York **2008**, pp. 839.
- [32] V. T. Srikar, S. M. Spearing, *Exp. Mech.* **2003**, *43*, 238.
- [33] J. Y. Chung, J.-H. Lee, K. L. Beers, C. M. Stafford, *Nano Lett.* **2011**, *11*, 3361.
- [34] M. Gunda, P. Kumar, M. Katiyar, *Crit. Rev. Solid State Mater. Sci.* **2016**, *42*, 129.
- [35] X. Li, D. Diao, B. Bhushan, *Acta Mater.* **1997**, *45*, 4453.
- [36] M. Hardiman, T. J. Vaughan, C. T. McCarthy, *Compos. Struct.* **2017**, *180*, 782.
- [37] G.-Y. Li, Y. Cao, *J. Acoust. Soc. Am.* **2017**, *142*, 1526.
- [38] A. A. Pelegri, X. Huang, *Compos. Sci. Technol.* **2008**, *68*, 147.
- [39] W. C. Oliver, G. M. Pharr, *J. Mater. Res.* **1992**, *7*, 1564.
- [40] R. Saha, W. D. Nix, *Acta Mater.* **2002**, *50*, 23.
- [41] R. Saha, Z. Xue, Y. Huang, W. D. Nix, *J. Mech. Phys. Solids* **2001**, *49*, 1997.
- [42] C. Lee, X. Wei, J. W. Kysar, J. Hone, *Science* **2008**, *321*, 385.
- [43] A. Falin, Q. Cai, E. J. G. Santos, D. Scullion, D. Qian, R. Zhang, Z. Yang, S. Huang, K. Watanabe, T. Taniguchi, M. R. Barnett, Y. Chen, R. S. Ruoff, L. H. Li, *Nat. Commun.* **2017**, *8*, 15815.
- [44] www.code-aster.com (accessed: June 2022).
- [45] S. Timoshenko, *Theory of Plates and Shells*, McGraw-Hill, New York **1959**.
- [46] K. Zhang, F. W. Si, H. L. Duan, J. Wang, *Acta Biomater.* **2010**, *6*, 2165.
- [47] F. K. Ko, J. Jovicic, *Biomacromolecules* **2004**, *5*, 780.
- [48] D.-N. Kim, F. J. Montáns, K.-J. Bathe, *Comput. Mech.* **2009**, *44*, 651.
- [49] I. Schmidt, *Comput. Mater. Sci.* **2005**, *32*, 518.
- [50] E. Car, S. Oller, E. Oñate, *Comput. Methods Appl. Mech. Eng.* **2000**, *185*, 245.
- [51] Han, *Continuum Mechanics and Plasticity*, Chapman & Hall/CRC, Boca Raton, FL **2005**.
- [52] N. Du, Z. Yang, X. Y. Liu, Y. Li, H. Y. Xu, *Adv. Funct. Mater.* **2010**, *21*, 772.
- [53] M. K. Chaudhury, T. Weaver, C. Y. Hui, E. J. Kramer, *J. Appl. Phys.* **1996**, *80*, 30.
- [54] J. Zhang, S. Du, A. Kafi, B. Fox, J. L. Li, X. Y. Liu, R. Rajkhowa, X. G. Wang, *RSC Adv.* **2015**, *5*, 1640.
- [55] S. Ling, C. Li, K. Jin, D. L. Kaplan, M. J. Buehler, *Adv. Mater.* **2016**, *28*, 7783.
- [56] Q. Wang, S. Ling, Q. Yao, Q. Li, D. Hu, Q. Dai, D. A. Weitz, D. L. Kaplan, M. J. Buehler, Y. Zhang, *ACS Mater. Lett.* **2020**, *2*, 153.
- [57] M. Stolz, R. Gottardi, R. Raiteri, S. Miot, I. Martin, R. Imer, U. Staufer, A. Raducanu, M. Duggelin, W. Baschong, A. U. Daniels, N. F. Friederich, A. Aszodi, U. Aebi, *Nat. Nanotechnol.* **2009**, *4*, 186.
- [58] A. N. Annaidh, K. Bruyère, M. Destrade, M. D. Gilchrist, M. Otténio, *J. Mech. Behav. Biomed. Mater.* **2012**, *5*, 139.
- [59] H. Joodaki, M. B. Panzer, *J. Eng. Med.* **2018**, *232*, 323.
- [60] T. D. Nguyen, B. L. Boyce, *Biomech. Model. Mechanobiol.* **2010**, *10*, 323.
- [61] P. M. Pinsky, D. van der Heide, D. Chernyak, *J. Cataract Refract. Surg.* **2005**, *31*, 136.
- [62] H.-Y. Zhou, Y. Cao, J. Wu, W.-S. Zhang, *Int. J. Ophthalmol.* **2017**, *10*, 803.
- [63] Y. M. Eftremov, M. Velay-Lizancos, C. J. Weaver, A. I. Athamneh, P. D. Zavattieri, D. M. Suter, A. Raman, *Sci. Rep.* **2019**, *9*, 5757.
- [64] D.-H. Kim, A. J. Ewald, J. Park, Kshitiz, M. Kwak, R. S. Gray, C.-Y. Su, J. Seo, S. S. An, A. Levchenko, *Sci. Rep.* **2018**, *8*, 14210.
- [65] D. Haskett, G. Johnson, A. Zhou, U. Utzinger, J. V. Geest, *Biomech. Model. Mechanobiol.* **2010**, *9*, 725.
- [66] C. Giordano, R. J. H. Cloots, J. A. W. van Dommelen, S. Kleiven, *J. Biomech.* **2014**, *47*, 1052.
- [67] B. E. V. Beers, J.-L. Daire, P. Garteiser, *J. Hepatol.* **2015**, *62*, 690.
- [68] Z. Liu, Z. Zhang, R. O. Ritchie, *Adv. Funct. Mater.* **2020**, *30*, 1908121.
- [69] C. Giordano, S. Zappalà, S. Kleiven, *Biomech. Model. Mechanobiol.* **2017**, *16*, 1269.
- [70] J. E. Sader, J. W. M. Chon, P. Mulvaney, *Rev. Sci. Instrum.* **1999**, *70*, 3967.
- [71] L.-O. Heim, M. Kappl, H.-J. Butt, *Langmuir* **2004**, *20*, 2760.
- [72] J. L. Hutter, *Langmuir* **2005**, *21*, 2630.
- [73] B. Cappella, G. Dietler, *Surf. Sci. Rep.* **1999**, *34*, 1.
- [74] H. Schniepp, D. Perera, Q. Wang, *Harvard Dataverse*, **2022**, V1, <https://doi.org/10.7910/DVN/LUEV5J>.